One-Step Coating of a ZnS Nanoparticle/MoS2Nanosheet Composite on Supported ZnO Nanorods as Anodes for Photoelectrochemical Water Splitting

Fareza, Ananta R.; Nugroho, Ferry Anggoro Ardy; Fauzia, Vivi

published in
ACS Applied Nano Materials
2022

DOI (link to publisher)
10.1021/acsanm.2c01434

document version
Publisher's PDF, also known as Version of record

ACS APPLIED NANO MATERIALS

www.acsanm.org Article

One-Step Coating of a ZnS Nanoparticle/MoS_2 Nanosheet Composite on Supported ZnO Nanorods as Anodes for Photoelectrochemical Water Splitting

Ananta R. Fareza, Ferry Anggoro Ardy Nugroho, and Vivi Fauzia*

Cite This: *ACS Appl. Nano Mater.* 2022, 5, 16051−16060 Read Online

ACCESS | Metrics & More | Article Recommendations | Supporting Information

ABSTRACT: ZnO-based photoanodes absorb a limited spectrum of light, and their photogenerated electrons and holes combine easily. Such features limit their photoelectrochemical activity. Herein, we report the synthesis of ternary heterostructures comprising ZnO nanorods (NRs) and ZnS nanoparticles wrapped in MoS_2 nanosheets (ZnO/ZnS/MoS_2, ZSM) directly grown on a substrate by a low-cost hydrothermal route and their performance as anodes for photoelectrochemical water splitting. The ZSM heterostructures exhibit a sixfold photocurrent density of 0.72 mA cm^{-2}, a fourfold maximum applied bias photon-to-current efficiency of 0.28% compared to bare ZnO NRs, and excellent photostability. These improvements in the overall photoelectrochemical activity are due to enhanced light absorption in the visible light range, higher surface active sites, and efficient charge separation enabled by the introduction of a ZnS/MOS_2 coating. Our study demonstrates an alternative architecture design of ternary heterostructures with increased photoelectrochemical activity. In general, this approach of constructing a double heterojunction can also be extended to other materials with similar architectures.

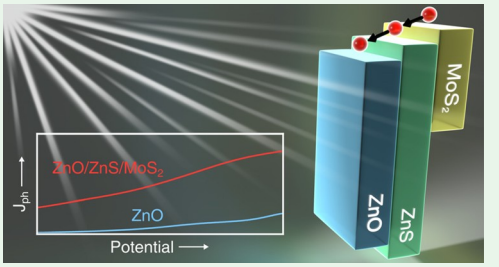

KEYWORDS: *ZnO/ZnS/MoS_2, ternary heterostructure, light absorption, charge recombination, photocurrent density, water oxidation, oxygen evolution reaction*

INTRODUCTION

Hydrogen gas has emerged as a main candidate for clean energies due to its lightweight nature with high energy density.[1] Apart from being a fuel, hydrogen can also be utilized to produce added-value goods, including ethanol, acetate, and methane.[2] However, around 96% of the current global hydrogen production is still generated from fossil fuels.[1] In response, research on hydrogen production using clean and renewable energy sources such as solar and water continues to grow. Water can be split into hydrogen and oxygen molecules using energy provided by the sun using a mechanism known as photoelectrochemical (PEC) water splitting. A basic PEC water splitting device employs two electrodes: a semiconductor-based photoanode and a metal cathode.[3] When these two electrodes are immersed in an electrolyte and exposed to sunlight, excitons (pairs of electrons and holes) are generated. The holes move to the photoanode surface to conduct oxygen evolution reaction (OER), while electrons migrate toward the metal cathode surface through a conductive wire to perform hydrogen evolution reaction (HER).[4,5]

To this end, an n-type semiconductor ZnO has been widely used as an OER photoanode due to its favorable band structure, which is close to the OER potential barrier of 1.23 V versus normal hydrogen electrode (NHE), thus preventing the impractical OER overpotential.[6−8] ZnO is also easy to synthesize via low-cost fabrication methods, including hydrothermal,[9] chemical bath deposition,[10] electrodeposition,[11] and sol−gel methods.[12] However, ZnO can only work optimally in the UV region owing to its wide band gap of 3.37 eV (equivalent to optical absorption at a wavelength of 368 nm).[13] This limited absorption window causes the ZnO-based photoanode to be less effective for PEC water splitting because 43% of the sunlight lies within the visible light range (380−740 nm).[14] In addition, the use of a monolithic semiconductor increases the recombination rate of the photogenerated electrons and holes, thus reducing the redox reaction.[3] To this end, heterostructure formation of a semiconductor with other semiconductor(s) is one appealing approach to reduce such charge recombination. This way, the photoexcited electrons and holes are transferred into a different material in the heterostructure, suppressing the recombination probability[4] and prolonging the electrons' lifetime.[15] The utilization of other semiconductors may also induce lattice mismatch in their interfaces, which consequently

Received: April 2, 2022
Accepted: June 14, 2022
Published: June 23, 2022

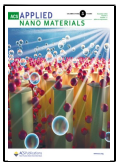

alters their band gaps and expands their light absorption range.[16,17]

In such concept, heterostructures comprising semiconductors with narrow and wide band gaps are ideal to prompt photogenerated charge movement and widen the light absorption range. For this reason, two-dimensional (2D) materials with a layered structure of molybdenum disulfide (MoS_2) have emerged as a novel standalone and/or an integrant photoelectrode in a PEC system.[8,16,18] For ZnO/MoS_2 heterostructures, such a combination has resulted in increased light scattering and absorption,[15,19,20] reduced band gap with maintained charge mobility,[21,22] and improved charge separation due to the lattice mismatch.[23,24] To this end, ZnO/MoS_2 heterostructure photoanodes have been fabricated using various methods from drop-casting[25] to solvothermal[26] and metal−organic chemical vapor deposition.[27,28] In such a structure, diverse ZnO morphologies have been utilized, namely, nanoparticles (NPs),[28] nanorods (NRs),[26,27] and nanowires (NWs).[25]

With the above results, it is possible to further elevate the PEC activity via charge movement engineering, achieved by incorporating an additional semiconductor with an appropriate band structure, for example, by forming a ternary heterostructure. When the process is done correctly, electrons and holes can be spatially confined through creation of electron and hole sinks, which results in enhanced charge separation.[29,30] Furthermore, a ternary heterostructure allows the formation of multiple interfaces with lattice mismatch, which modifies the band gap[21,22] and the absorbance of the heterostructure, as discussed above.

Fortunately, it is possible to form ternary heterostructures with ease due to in situ nucleation during hydrothermal synthesis, typically from excess precursors. In MoS_2 synthesis using a hydrothermal route, several authors reported the formation of various integrants, such as Ni_3S_2[31] or NiS_2[32] (excess sulfur reacts with nickel foam), CoS_2[33] (excess sulfur reacts with cobalt), and ZnS[15,20] (excess sulfur reacts with zinc). Specific to ZnS, a prior study reported charge recombination inhibition and photocatalytic activity improvement in ZnO/ZnS/MoS_2 nanoarrays synthesized using two hydrothermal processes.[20] In another example, ZnO/ZnS/MoS_2 nanostructured powder exhibited an improved photocatalytic HER, which was attributed to in situ-generated ZnS that increased the number of interfaces.[15] Additionally, a photocurrent density (J_{ph}) as high as 5.23 μA cm^{-2} at 0 V versus Ag/AgCl was achieved by binding the nanopowder with Nafion followed by drop-casting on top of an ITO substrate. However, such an approach may infer PEC activity reduction due to the intrinsic charge resistance of the binder. The resulting ZnO orientation was also highly randomized since there was no immobilized platform (i.e., ZnO seed) on the substrate's surface for ZnO to grow vertically. This lack of the ZnO seed layer hinders charge transfer from the active materials toward the conductive substrate. These drawbacks simultaneously cause unsatisfactory PEC activity, and thus a better architecture design of such a heterostructure is necessary.

As a response, herein, we develop a photoanode composed of vertically aligned ZnO/ZnS/MoS_2 (ZSM), where the ZnS nanoparticles/MoS_2 nanosheets (NSs) coating is achieved through a single-step hydrothermal process on directly grown ZnO nanorods on a fluorine-doped tin oxide (FTO) substrate. This binder-free and directly grown approach allows intimate contact of the heterostructures with the conductive substrate via the ZnO seed layer, which promotes charge transfer. As a result, a photoanode with a J_{ph} of 0.72 mA cm^{-2} at 1.23 V versus reversible hydrogen electrode (RHE) and excellent photostability is obtained. This excellent performance is attributed to the enhanced charge separation driven by the formation of double heterojunctions between ZnO/ZnS and ZnS/MoS_2.

EXPERIMENTAL SECTION

Synthesis of ZSM. Scheme 1 illustrates the steps taken to produce the ZSM heterostructures. First, ZnO NRs were fabricated using two successive steps, namely, seeding and growth. First, 0.2 M zinc acetate dihydrate ($Zn(CH_3COO)_2{\cdot}2H_2O$) dissolved in deionized water was poured into a 1.7 MHz atomic nebulizer to spray the FTO-coated glass substrate for 15 min. Prior to this, the glass was preannealed at 450 °C for 10 min in an air atmosphere to facilitate nucleation of the ZnO seed. To induce ZnO growth, the sprayed sample was placed 45° upside down in an aqueous growth solution comprising of 20 mL of equimolar 0.05 M zinc nitrate tetrahydrate ($Zn(NO_3)_2{\cdot}4H_2O$) and hexamethylenetetramine ($C_6H_{12}N_4$) for 6 h at 95 °C in an electric oven. Finally, the ZSM heterostructures were synthesized using a modified approach from a prior study[34] in which the ZnO NRs were placed 45° upside down in an aqueous solution containing 0.02 M sodium molybdate dihydrate ($Na_2MoO_4{\cdot}2H_2O$) and 0.13 M thioacetamide (CH_3CSNH_2) in deionized water and heated at a temperature of 200 °C for 24 h in a Teflon-lined stainless steel

Scheme 1. Artist's Rendition of ZSM Heterostructure Fabrication Comprising ZnO Seed Layer Deposition on an FTO Substrate, ZnO Seed Layer Growth into ZnO NRs, and Concurrent in Situ Synthesis and Deposition of ZnS and MoS_2 on ZnO NRs' Surface

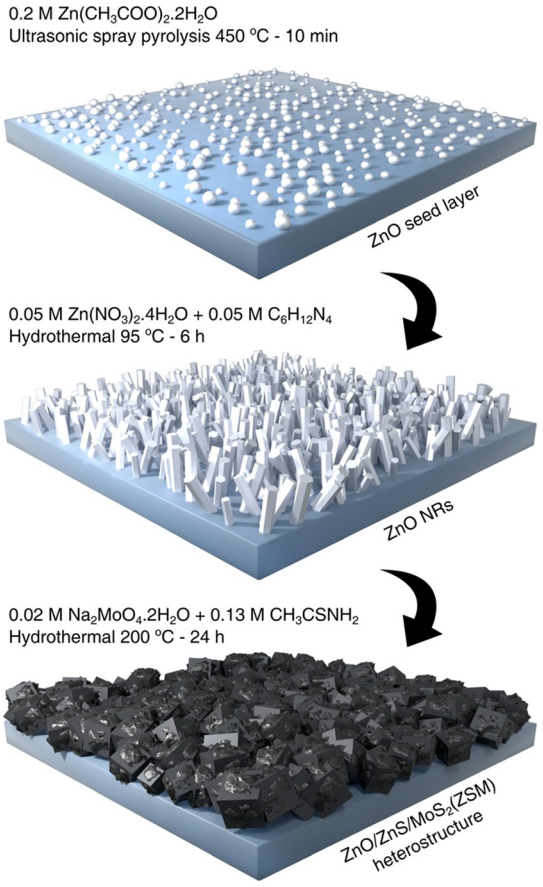

https://doi.org/10.1021/acsanm.2c01434
ACS Appl. Nano Mater. 2022, 5, 16051−16060

autoclave. The simultaneous formation of ZnS and MoS_2 on the surface of ZnO occurs according to the following reaction equations[35,36]

$$2CH_3CSNH_2 + 4H_2O \rightarrow 2NH_3 + 2CH_3COOH + 2H_2S \quad (1)$$

$$H_2S + ZnO \rightarrow ZnS + H_2O \quad (2)$$

$$4MoO_4^{2-} + 9H_2S + 6CH_3COOH \rightarrow 4MoS_2 + SO_4^{2-} + 6CH_3COO^- + 12H_2O \quad (3)$$

Material Characterizations and PEC Measurements. X-ray diffraction (XRD) measurements were carried out using a Panalytical X'Pert Pro diffractometer with CuKα radiation (λ = 1.54 Å), while the samples' morphology was characterized using a field-emission scanning electron microscope (FESEM) Hitachi SU-8030 and a high-resolution transmission electron microscope (HRTEM)−EDX FEI Tecnai G20 S-Twin at 200 kV beam exposure. Samples' optical absorption was measured by the Thermo Fisher Scientific GENESYS 10S UV−vis spectrophotometer. The ULVAC-PHI Quantera II spectrophotometer collected the X-ray photoelectron spectroscopy (XPS) spectra with the Al Kα X-ray beam at 1486.6 eV. The current−potential measurement was recorded by an Autolab PGSTAT204 potentiostat in a three-electrode electrochemical workstation system using 0.5 M Na_2SO_4 (pH = 6.8) as the electrolyte. The device was illuminated with a solar simulator paired with an AM 1.5G filter and calibrated using a solar power meter SM206 to establish a light intensity of 75 mW cm^{-2}. The samples with an active area of 1 cm^2 were used as the working electrode, Pt electrode was used as the counter electrode, and Ag/AgCl (saturated 3.0 M KCl aqueous solution) was used as the reference electrode. The current−time measurement was recorded under continuous solar simulator irradiance for 1800 s with a constant bias of 1.23 V versus RHE. The impedance measurement was recorded without illumination using sine waves (0.1−100,000 Hz). The applied bias of the Ag/AgCl electrode (V vs Ag/AgCl) was then converted into the reversible hydrogen electrode (V vs RHE) using the Nernst equation

$$E\ (V \text{ vs RHE}) = E\ (V \text{ vs Ag/AgCl}) + (0.059 \times \text{pH}) + 0.21 \quad (4)$$

RESULTS AND DISCUSSION

Crystallography Analysis. To validate the phase composition of our synthesized samples, we carried out XRD measurements. Figure 1 shows the XRD pattern of bare ZnO, revealing the facets of (002), (101), (102), (103), and (112) in the wurtzite phase.[9,10] From the pattern, we deduced the (002) facet interplanar spacing of 0.27 nm. For the ZSM sample, we noticed a similar pattern but with two additional peaks that correspond to the (111) and (022) zinc blende ZnS. The interplanar spacing of the (111) ZnS plane is found to be 0.33 nm. Notably, the ZSM sample shows no diffraction peaks corresponding to the standard MoS_2 reference. Such an absence is likely due to the inability of conventional XRD instruments with the Bragg−Brentano geometry to examine the ultrathin 2D MoS_2 layers.[37] However, its presence was confirmed by an XPS measurement, which will be discussed later below.

From the XRD patterns, it is evident that the semipolar (101) facet is the dominant facet in the ZnO sample, which originates from the nonuniform polarity of the ZnO seed layer.[38] Being a semipolar facet, (101) ZnO exhibits a lower surface energy (6.51 J m^{-2}) compared to its polar (002) counterpart (12.42 J m^{-2}),[39] which mirrors its reactivity with water molecules. On the other hand, the polar (111) ZnS facet dominates in the ZSM sample. Such a facet is reported to have

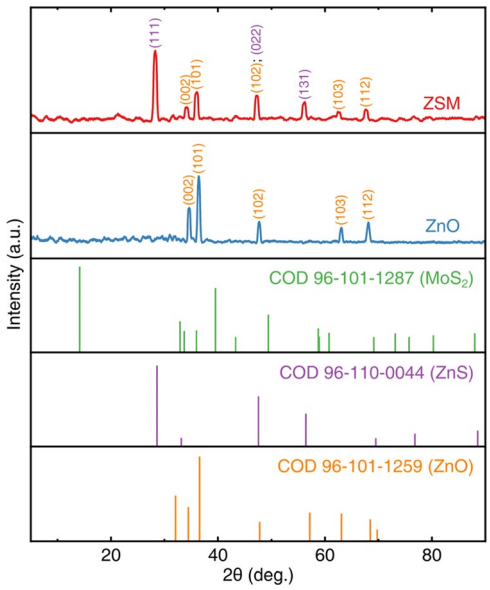

Figure 1. XRD patterns of ZnO and ZSM samples along with COD 96-101-1259 (ZnO), COD 96-110-0044 (ZnS), and COD 96-101-1287 (MoS_2) references. The ZnO sample shows expected diffraction peaks with a dominant (101) facet, while the ZSM sample exhibits a combination of diffraction peaks between ZnO and ZnS. The absence of expected MoS_2 diffraction peaks in the ZSM sample is due to the limitation of conventional XRD instruments to examine ultrathin 2D materials.

the lowest water adsorption energy of −1.06 eV,[40] thus stronger electronic interactions with water molecules.

Microscopic Analysis. Next, we investigated the microstructure of our samples. Figure 2a,b show the representative FESEM and TEM images of the synthesized, vertically aligned ZnO NRs, respectively. The NRs are hexagonal with an average side-to-side diameter of 124.7 nm. Through the high-resolution TEM image, we found an interplanar spacing of 0.26 nm, which can be attributed to the (002) ZnO, based on the XRD data mentioned above (Figure 2c). On the other hand, Figure 2d,e show the morphology of ZSM with the existence of irregular NPs with an average diameter of 124.4 nm, which partially cover the ZnO NRs. These NPs are likely ZnS covered with a few-layer MoS_2 NSs. It is reported that the outer layer of ZnO NRs transforms into ZnS when there are sufficient sulfur precursor concentration and reaction time.[41,42] The partial transformation of ZnO to ZnS can be seen as a few ZnO NRs maintain their hexagonal rod morphology, while the rest convert into ZnS with a cube-like morphology, confirming a fair degree of sulfidation in the ZSM sample. In our case, the emergence of ZnS originates from the sulfur in CH_3CSNH_2 that reacts with ZnO NRs. Furthermore, there is excess sulfur that reacts with $Na_2MoO_4{\cdot}2H_2O$ and materializes into low-density MoS_2 NSs. These few-layer MoS_2 NSs concentrate and encapsulate the outer layer of ZnO/ZnS, forming ZSM heterostructures. To confirm the existence of these three phases, we employed a high-resolution TEM that reveals three distinct lattice fringes that correspond to ZnO, ZnS, and MoS_2 (Figure 2f). Specifically, the interlayer spacing of 0.69 nm corresponds to (002) MoS_2, while those of 0.32 and 0.26 nm are in good agreement with the facets of (111) ZnS and (002) ZnO, respectively. These values are consistent with our findings on the crystallography analysis above.

https://doi.org/10.1021/acsanm.2c01434
ACS Appl. Nano Mater. 2022, 5, 16051−16060

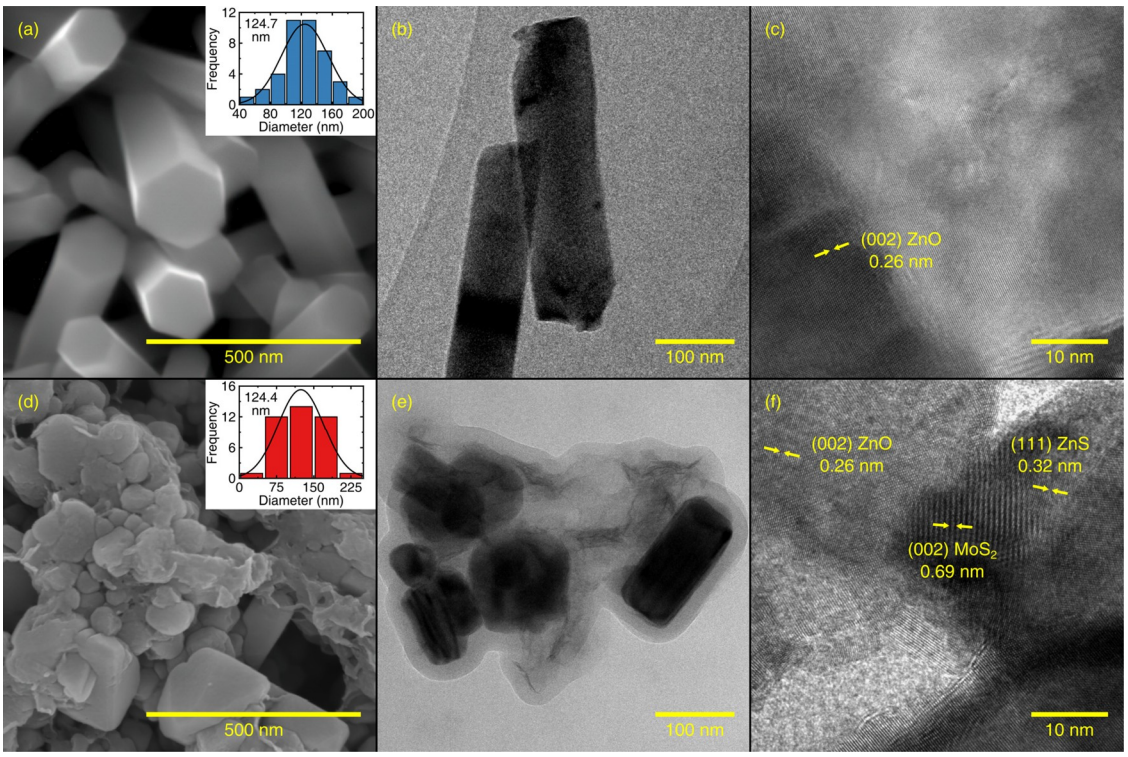

Figure 2. (a) FESEM image, (b) TEM image, and (c) HRTEM image of ZnO NRs. The inset in panel (a) shows the side-to-side diameter distribution histogram of ZnO NRs. (d) FESEM image, (e) TEM image, and (f) HRTEM image of ZSM heterostructures. The found interlayer spacings correspond excellently with the facets of (002) ZnO, (111) ZnS, and (002) MoS_2, corroborating the formation of ZSM heterostructures. The inset in panel (d) shows the diameter distribution histogram of ZnS NPs.

Spectroscopic Analysis. To investigate the optical properties, the UV−vis absorbance of all samples was recorded within 300−800 nm (Figure 3a). It is clear that ZSM's absorbance in the visible range is considerably higher than that of bare ZnO owing to the presence of ZnS NPs with a higher surface area and the absorption contribution by MoS_2 NSs.[15,20] There is also a hint of band gap reduction in ZSM as its absorption edge redshifts from 386 to 400 nm, compared to bare ZnO. By constructing a Tauc plot, we found that ZSM exhibits a 3.10 eV band gap, which is considerably lower than that of bare ZnO of 3.21 eV (Figure 3b). From the crystallography and microscopic analysis above, the three compositing materials have different lattice types (i.e., hexagonal ZnO, cubic ZnS, and hexagonal MoS_2). These lattice disparities comprising hexagonal/cubic/hexagonal interfaces result in substantial lattice mismatch and thus generate compressive and tensile strains at the interfacial areas that contribute to band gap tuning.[21,22]

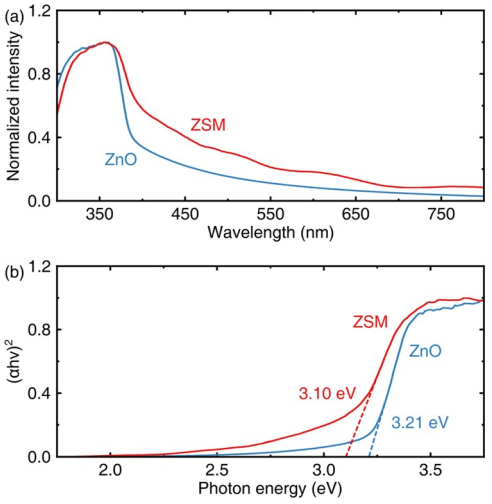

Figure 3. Optical properties of ZnO and the ZSM heterostructure. (a) UV−vis absorbance spectra. (b) Corresponding Tauc plot. Light absorption enhancement in the visible range is observed for ZSM with a lower band gap than ZnO.

In the next step, we conducted XPS measurement to determine the surface chemical composition and oxidation state of all the elements in our samples. From the obtained spectra, we make the following observation (see Table S1 for the list of the peak energies): (i) ZnO and ZSM samples exhibit the signature features of Zn and O (Figure 4a,b). (ii) At the Zn 2p region, the ZnO peaks are split into two, which correspond to Zn $2p_{3/2}$ and Zn $2p_{1/2}$ states, respectively (Figure 4a).[43] The difference of ∼23 eV between the peaks confirms that the Zn ions are in a +2 oxidation state.[43,44] (iii) For ZSM, the Zn 2p peaks are shifted to a higher energy, indicating the presence of ZnS bonds.[45] (iv) The peak in the O 1s spectrum of bare ZnO is deconvoluted into three peaks: O1 peak corresponding to the O^{2-} state of lattice oxygen in wurtzite ZnO, O2 peak correlating to the oxygen vacancies V_O, and O3 peak corresponding to the adsorbed −OH molecules or other surface oxygen species (Figure 4b).[43,46] (v) For ZSM, the O 1s spectra comprise a low-intensity O1 peak due to ZnO being partially covered by ZnS NPs. This is further supported by the O2 peak shift to a higher binding energy, which correlates with the formation of ZnS.[47,48] On the other hand, the O3 peak is higher in intensity, indicating a higher active site for the adsorption of −OH molecules, which is beneficial

https://doi.org/10.1021/acsanm.2c01434
ACS Appl. Nano Mater. 2022, 5, 16051−16060

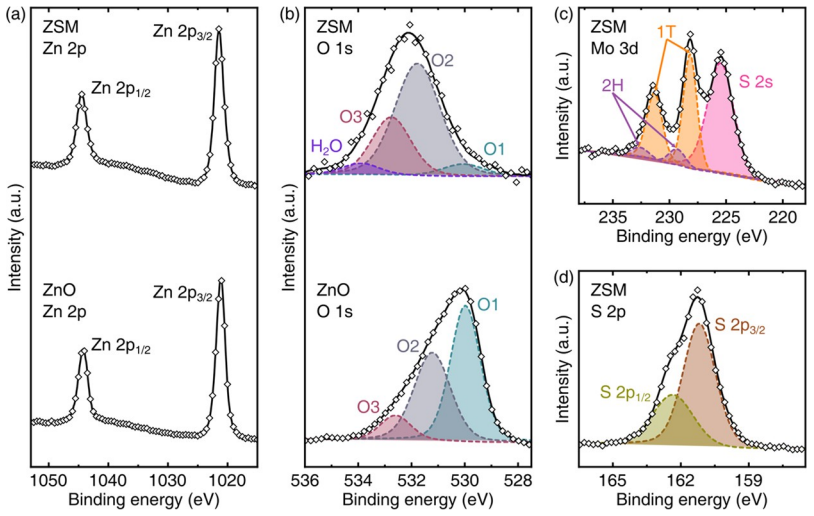

Figure 4. XPS spectra at core levels of (a) Zn 2p, (b) O 1s, (c) Mo 3d, and (d) S 2p. The peak splitting at the Mo 3d region signifies a mixed 1T/2H MoS_2 polytype existing with a high density of 1T MoS_2 (86.1%).

for PEC activity. (vi) ZSM contains a mixed metallic 1T and semiconducting 2H MoS_2 polytypes (Figure 4c).[49] (vii) In the S 2p region of ZSM, there are two peaks of S $2p_{1/2}$ and S $2p_{3/2}$, which are attributed to the S^{2-} state in ZnS and MoS_2 phases, respectively (Figure 4d).[45,50] By deconvoluting and calculating these peaks, we found MoS_2 in the heterostructure to comprise 86.1% of 1T MoS_2 phase.

Performance Benchmark. Having confirmed the existence of a ZnS/MoS_2 coating in our heterostructures, we set out to investigate its effect on the PEC activity when used as a photoanode. The PEC measurements of the ZSM heterostructures were conducted by performing linear sweep voltammetry (LSV) measurements under 75 mW cm^{-2} solar simulator illumination with 0.5 M Na_2SO_4 as the electrolyte and were compared to its bare ZnO counterpart, as shown in Figure 5a. Because of limited light absorption and severe charge recombination, ZnO registers a low J_{ph} at 1.23 V versus RHE of 0.12 mA cm^{-2}. On the contrary, ZSM shows a sixfold J_{ph} improvement of 0.72 mA cm^{-2}. Furthermore, the ratio of energy converted under illumination while applying bias is described as the applied bias photon-to-current efficiency (ABPE)

$$\mathrm{ABPE} = \frac{(J_{ph})(1.23\ \mathrm{V} - V_b)}{P} \times 100\% \quad (5)$$

where J_{ph} is the photocurrent density (mA cm^{-2}), V_b is the applied bias (V), and P is the intensity of solar illumination (75 mW cm^{-2}). Figure 5b shows the ABPE of the samples, where ZSM displays a maximum ABPE of 0.28% at 0.43 V versus RHE due to more efficient charge separation. Meanwhile, ZnO only exhibits a much lower maximum ABPE of 0.06% at 0.90 V versus RHE. We also noticed a shift in the potential where the maximum ABPE occurred (from 0.90 to 0.43 V vs RHE), likely caused by the reduced overpotential in ZSM.

For real applications, stability is an important parameter for a device. Hence, in Figure 5c, we show the recorded CA curves of continuous J_{ph} of ZSM and ZnO samples over 30 min of operational time. It is evident that ZSM exhibits better stability than its ZnO counterpart. In particular, over the course of 30 min, ZSM only experiences a minor J_{ph} decay of 3% from the initial value. In contrast, ZnO exhibits a significant 17% J_{ph} decrease over the same duration. We argue such deterioration to occur due to photocorrosion in ZnO. In particular, the accumulated holes oxidize the oxygen atoms in ZnO instead of the ones in water. This way, zinc ions are released via the reaction $2ZnO + 4h^+ \rightarrow 2Zn^{2+} + O_2$, initiating structural

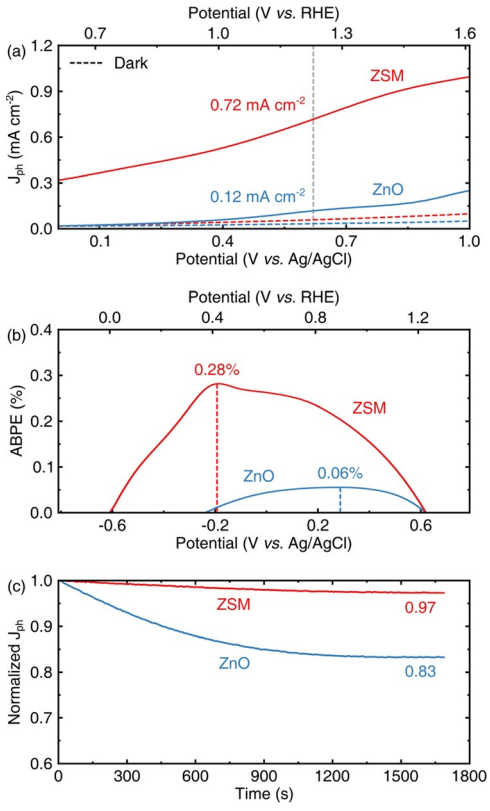

Figure 5. PEC measurement of ZnO and ZSM samples in a standard three-electrode electrochemical workstation system. (a) LSV curves under 75 mW cm^{-2} illumination using a 0.5 M Na_2SO_4 electrolyte. The gray dashed line denotes the benchmarking potential of 1.23 V vs RHE, while the blue and red dashed lines correspond to the dark current. (b) Corresponding ABPE curves with dashed lines representing the maximum ABPE. (c) Chronoamperometry (CA) curves under constant irradiance (75 mW cm^{-2}) and bias (1.23 V vs RHE) over time.

https://doi.org/10.1021/acsanm.2c01434
ACS Appl. Nano Mater. 2022, 5, 16051−16060

decomposition.[51] In the ZSM sample, such a reaction does not take place due to ZnO being effectively passivated by the ZnS/MoS_2 coating.

Next, we investigate the charge separation dynamics of ZnO and ZSM samples using electrochemical impedance spectroscopy (EIS) measurement with sine waves of 0.1−100,000 Hz under dark conditions. Figure 6a depicts the Nyquist plot of

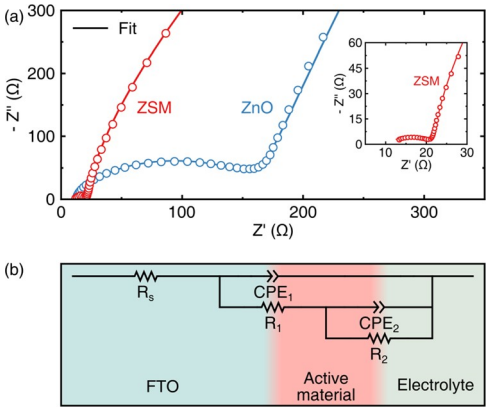

Figure 6. (a) Nyquist plot under dark conditions using a 0.5 M Na_2SO_4 electrolyte and 0.1−100,000 Hz sine waves showing the measured and fitted data. The inset shows the magnified Nyquist plot of the ZSM heterostructure. (b) Equivalent circuit used for data fitting, where R_s denotes the ohmic resistance, R_1 indicates the charge-transfer resistance across the photoanode, and R_2 represents the oxygen adsorption/desorption and oxygen ion diffusion on the photoanode's surface. CPE_1 and CPE_2 refer to the corresponding dispersive resistance factors of R_1 and R_2, respectively.

ZnO and ZSM samples. Both ZnO and ZSM show a semicircle shape that signifies an imperfect capacitive characteristic. Thus, instead of using the double-layer capacitance (C_{dl}), the constant phase element (CPE) is applied to resolve the dispersive capacitance across the surface of the samples. We then fit the measured EIS spectra using the equivalent circuit shown in Figure 6b, where R_s is the ohmic resistance comprising ionic and electronic components, R_1 and R_2 are the charge-transfer resistances between FTO/active material[52] and oxygen adsorption/desorption and oxygen ion diffusion from the electrolyte into the photoanode's surface,[53] respectively, and CPE_1 and CPE_2 are the corresponding dispersive resistance factors of R_1 and R_2. The complete impedance parameters used for fitting are listed in Table S2. The arcs in the high frequency denote the R_s of ZnO (11.54 Ω) and ZSM (7.97 Ω). Evidently, ZSM exhibits a smaller R_1 and R_2 than ZnO (16.32 Ω and 6.16 kΩ compared to 160.30 Ω and 14.96 kΩ, respectively). In both cases, R_1 is much lower than R_2, suggesting that the OER kinetics is highly influenced by oxygen adsorption/desorption and oxygen ion diffusion. This is due to the faster migration rate of holes into the photoanode/electrolyte interface compared to the hole injection rate to the electrolyte, thus resulting in a sluggish OER kinetics.[8] Undoubtedly, the high reduction in the R_1 and R_2 values signifies faster charge transfer and oxygen adsorption/desorption in ZSM. The Nyquist plot also contains information about real impedance (Z') and imaginary impedance (Z'') components. One can determine the magnitude of these vectors in the form of total impedance ($|Z|$) as a function of frequency. Figure S1a displays a |Z| Bode plot from which we can infer that ZSM exhibits a higher electrochemical performance compared to ZnO, specifically in the high frequency regime (see related discussion in the Supporting Information). The sine waves in EIS measurements also carry information of the phase angle (ϕ). In OER specifically, holes act as minority carriers, where they move toward the surface of the photoanode. Since these carriers have limited lifetime, determining the holes' diffusivity from bulk to the surface is crucial. Here, we can determine the hole diffusion length (L_h) with the relation $L_h = \sqrt{D_h \tau_h}$, where D_h and τ_h are the hole diffusion coefficient and relaxation time, in which such information could be retrieved from the Bode ϕ plot (Figure S1b). We found that ZSM exhibits a shorter L_h of 25 μm compared to that of bare ZnO of 71 μm.

As a final characterization of the performance of our heterostructures, we conducted a Mott−Schottky (MS) analysis to investigate the charge separation in the photoanodes at 1 kHz frequency in the dark. As detailed in Figure S2, we found the flat-band potential (V_{fb}) of ZnO and ZSM to be −0.10 and 0.13 V versus RHE, respectively. Furthermore, the corresponding slope from the MS equation reveals the donor density (N_d), that is, 4.07×10^{12} and 1.83×10^{14} cm^{-3} for ZnO and ZSM, respectively. It is also worth noting that both ZnO and ZSM display a positive slope, indicating *n*-type conductivity. All of these properties of ZnO and ZSM based on the EIS analysis are summarized in Table 1.

Having characterized in detail the performance aspects of our samples, we now discuss the factors contributing to the overall OER activity improvement in ZSM compared to bare ZnO. To start, we note the emergence of the polar (111) ZnS facet in the ZSM sample (cf. Figure 1) with low water adsorption energy, facilitating stronger electronic interactions with water molecules. From the microscopy analysis, we also found increased structural complexity as ZnS and MoS_2 are grown on the ZnO NR surface, leading to increased surface area (cf. Figure 2d). Consequently, the light scattering in such complex structures is improved through recapturing of the reflected light.[19] This optical enhancement in ZSM is also clear in the increased visible range absorbance spectra (cf. Figure 3a), owing to the lattice mismatch between each interface, which in turn invokes band gap reduction and increases the light-harvesting ability.[21,22] In terms of impedance analysis, ZSM yields shorter L_h compared to bare ZnO. This phenomenon is in agreement with previous studies, where enlarged surface area (e.g., by establishing heterostructures in our case) leads to shorter L_h.[54,55] Shorter L_h is beneficial in that it enhances the charge separation and lowers the charge recombination event.[54,55] In addition to this, the positive shift found in the ZSM's V_{fb} signifies a higher degree of band

Table 1. Impedance Parameters of ZnO and ZSM Measured in 0.5 M Na_2SO_4 under Dark Conditions

sample	charge-transfer resistance, R_1 (Ω)	relaxation frequency, f_{max} (Hz)	relaxation time, τ (ms)	hole diffusion length, L_h (μm)	flat-band potential, V_{fb} (V vs RHE)	donor density, N_d (cm^{-3})
ZnO	160.30	1.26	126	71	−0.10	4.07×10^{12}
ZSM	16.32	10.00	16	25	0.13	1.83×10^{14}

https://doi.org/10.1021/acsanm.2c01434
ACS Appl. Nano Mater. 2022, 5, 16051−16060

Table 2. Performance Comparison of PEC Water Splitting Devices of Similar Heterostructures

materials	band alignment	electrolyte	light intensity (mW cm^{-2})	photocurrent density, J_{ph} at 1.23 V vs RHE (mA cm^{-2})	applied bias photon-to-current efficiency, ABPE (%)	ref
ZnO/ZnS	N.A.	0.5 M Na_2SO_4	50	0.40	0.26	58
ZnO/ZnS	type-II	0.5 M Na_2SO_4	100	0.60	0.23	59
ZnO/MoS_2	type-II	0.5 M Na_2SO_4	100	0.51	N.A.	25
ZnO/MoS_2	type-II	0.1 M Na_2S + H_2SO_4	100	N.A.	0.91	27
ZnO/ZnS/MoS_2	type-I/type-II	0.5 M Na_2SO_4	75	0.72	0.28	this work

bending phenomenon,[56,57] leading to minimized charge recombination at the photoanode/electrolyte interface. A higher N_d on ZSM results in higher conductivity in the photoanode/electrolyte interface, contributing to higher charge separation.[57] These multitude, synergistic enhancements in both light absorption and electrocatalysis activities materialize into higher overall OER activity. Finally, in terms of stability, ZSM experiences a marginal decay, proving that the encapsulation of ZnO with ZnS and MoS_2 substantially boosts the durability of the device. However, its structural integrity should be further investigated to achieve long-term operational PEC water splitting. To summarize, we compare our study to other similar heterostructures found in the literature in Table 2 where our ZSM sample shows, in particular for J_{ph}, an excellent OER performance compared to the binary counterparts even with an underpowered solar simulator intensity of only 75 mW cm^{-2} instead of the standardized 100 mW cm^{-2} intensity.

Charge-Transfer Mechanism. As the final analysis of our study, we propose the corresponding band structure of our ZSM heterostructures, which we argue as one of the contributing factors in our enhanced PEC water splitting activity, in particular, through the improved separation of the photogenerated carriers. The band structure comprising the conduction band (CB) and valence band (VB) positions of ZnO, ZnS, and MoS_2 is defined by[15]

$$\mathrm{CB} = X + E_0 - \frac{E_g}{2} \tag{6}$$

$$\mathrm{CB} = VB - E_g \tag{7}$$

where E_0 and E_g are the scale factor of the redox level versus NHE against the vacuum level (E_0 = −4.5 eV) and the band gap, respectively. X is the electronegativity (ZnO = 5.79 eV, ZnS = 5.26 eV, and MoS_2 = 5.32 eV[15,60]), while W is the work function (ZnO = 4.70 eV, ZnS = 4.11 eV, and MoS_2 = 5.39 eV[61,62]). Referring to V versus NHE, when an equilibrium state (i.e., under dark conditions) is achieved, we found CB_{ZnO}, VB_{ZnO}, CB_{ZnS}, VB_{ZnS}, CB_{MoS_2}, and VB_{MoS_2} to be −0.32, 2.89, −0.57, 3.27, −0.76, and 1.02 V, respectively. With these data, we construct the band diagram of our system as illustrated in Figure 7. The established band position and alignment expedite charge separation. During quasi-static equilibrium under illumination, the device requires ZnO, ZnS, and MoS_2 to reach the same Fermi level (E_F), including platinum as the counter electrode. In such a case, electrons moving from the photoanode typically occupy the E_F of the metal counter electrode. Since the overall E_F equilibrated below the HER potential, an additional applied bias is required to drive the whole reaction. We also noticed that the ZnS/MoS_2 interface displays type-II band alignment, where electrons from CB_{MoS_2} flow into CB_{ZnO}. In contrast, the interface of ZnO/ZnS shows type-I band alignment, where electrons from CB_{ZnS} migrate into CB_{ZnO}, to FTO, and finally end at the surface of the platinum electrode to conduct HER. Meanwhile, holes in the VB of each material perform OER. Since electrons and holes are spatially confined, the charge recombination is significantly reduced.

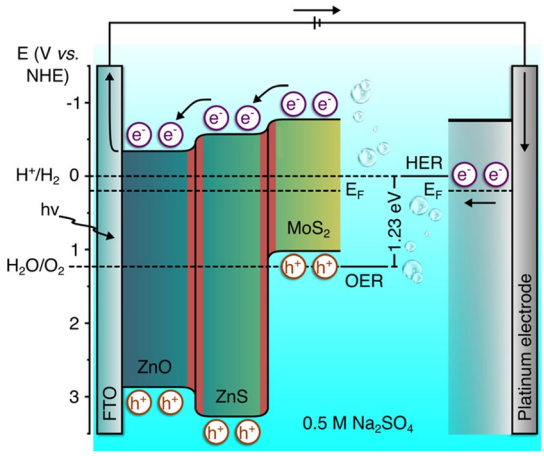

Figure 7. Proposed charge-transfer mechanism of the ZSM heterostructure indicating type-II band alignment at the ZnS/MoS_2 interface and type-I band alignment at the ZnO/ZnS interface. E_F and black arrow lines denote the Fermi level and the movement of photoexcited electrons, respectively. The spatially confined electrons and holes restrain the charge recombination and magnify the PEC activity.

We note a disparity in our band structure compared to previous studies based on photocatalytic water splitting, specifically the ones from the studies of Fu et al. (ZnS/ZnO/MoS_2 with type-II/type-II alignment)[20] and Lee et al. (ZnO/ZnS/MoS_2 with type-II/type-I alignment).[63] At this point, it is worth mentioning that Fu et al.'s band alignment will turn into type-II/type-I alignment when ZnO and ZnS switch places. In such a case, the photoexcited electrons move from the CB of ZnS into ZnO and MoS_2, while holes accumulate in the VB of MoS_2. This condition is not a problem for suspended particle-based photocatalytic water splitting (as in the studies of Fu et al.[20] and Lee et al.[63]) since electrons perform water reduction immediately at the catalyst surfaces. In our case, however, the photoexcited electrons must move into the conductive substrate (i.e., FTO) and settle at the platinum electrode to carry out HER. If we employ the band structure proposed by Fu et al. and Lee et al., electrons from the CB of MoS_2 cannot move into the FTO since the CB of ZnS impedes the electron path. This blocking potentially leads to charge recombination and thus a lower J_{ph}. However, this is not the case in our study where we observed an increase in overall PEC activity in the ZSM sample compared to bare ZnO. To this end, differences in band structure, even in systems with identical constituting materials synthesized using

https://doi.org/10.1021/acsanm.2c01434
ACS Appl. Nano Mater. 2022, 5, 16051−16060

similar methods, are a common occurrence. This is particularly true for materials with CB and/or VB positions located at a very close level. This is further substantiated by the fact that the band structure is highly sensitive to, among others, the density of defect and/or doping (e.g., oxygen vacancies and nonmetal doping), and the electrolyte used, typically in the impedance-based measurement. Therefore, a slight modification in synthesis and measurement parameters (intentionally or not) is likely to affect the band structure and alignment of the materials. Further example includes ZnO/MoS_2 heterostructures where band alignments of type-I,[64] type-II,[25] and *p*–*n* junction[65] have been reported.

CONCLUSIONS

Photoanodes based on $ZnO/ZnS/MoS_2$ heterostructures for PEC water splitting were successfully synthesized via a hydrothermal route. The emergence of in situ ZnS NPs and few-layer MoS_2 NSs established the ZnO/ZnS and ZnS/MoS_2 interfaces, which facilitates higher light absorption in the visible range, enhances the surface active sites, and improves charge separation, altogether resulting in increased PEC activity and stability. In particular, the $ZnO/ZnS/MoS_2$ heterostructure registers a J_{ph} of 0.72 mA cm^{-2} at 1.23 V versus RHE, which is among the highest value reported for systems with similar materials, and a maximum ABPE of 0.28%, that is, over sixfold higher than that of bare ZnO NRs. Our study demonstrates a strategy to improve the PEC water splitting activity of a photoanode using simple and direct synthesis. On that account, the presented method of constructing a double heterojunction can be extended to other materials with a similar architecture, for example, ZnO/g-C_3N_4/CdS and TiO_2/CdS/PbS ternary heterostructures.

ASSOCIATED CONTENT

Supporting Information

The Supporting Information is available free of charge at https://pubs.acs.org/doi/10.1021/acsanm.2c01434.

Extended XPS data, fitting parameters to EIS measurement, Bode total impedance analysis, Bode phase angle analysis, and MS analysis (PDF)

AUTHOR INFORMATION

Corresponding Author

Vivi Fauzia − *Department of Physics, Universitas Indonesia, Depok 16424, Indonesia;* orcid.org/0000-0002-4593-4662; Email: vivi@sci.ui.ac.id

Authors

Ananta R. Fareza − *Department of Physics, Universitas Indonesia, Depok 16424, Indonesia;* orcid.org/0000-0002-2557-1382

Ferry Anggoro Ardy Nugroho − *Department of Physics and Astronomy, Vrije Universiteit Amsterdam, 1081 HV Amsterdam, The Netherlands*

Complete contact information is available at: https://pubs.acs.org/10.1021/acsanm.2c01434

Author Contributions

The manuscript was written through contributions of all authors. All authors have given approval to the final version of the manuscript.

Notes

The authors declare no competing financial interest.

ACKNOWLEDGMENTS

The work is supported by the Hibah Riset FMIPA UI 2021 NKB-037/UN2.F3/HKP.05.00/2021.

REFERENCES

(1) Shiva Kumar, S.; Himabindu, V. Hydrogen Production by PEM Water Electrolysis − A Review. *Mater. Sci. Energy Technol.* **2019**, *2*, 442−454.

(2) Asimakopoulos, K.; Gavala, H. N.; Skiadas, I. V. Reactor Systems for Syngas Fermentation Processes: A Review. *Chem. Eng. J.* **2018**, *348*, 732−744.

(3) Ahmed, M.; Dincer, I. A Review on Photoelectrochemical Hydrogen Production Systems: Challenges and Future Directions. *Int. J. Hydrogen Energy* **2019**, *44*, 2474−2507.

(4) Kahng, S.; Yoo, H.; Kim, J. H. Recent Advances in Earth-Abundant Photocatalyst Materials for Solar H2 Production. *Adv. Powder Technol.* **2020**, *31*, 11−28.

(5) Wu, H.; Tan, H. L.; Toe, C. Y.; Scott, J.; Wang, L.; Amal, R.; Ng, Y. H. Photocatalytic and Photoelectrochemical Systems: Similarities and Differences. *Adv. Mater.* **2020**, *32*, No. 1904717.

(6) Chen, Z.; Dinh, H. N.; Miller, E. *Photoelectrochemical Water Splitting*; Springer Briefs in Energy; Springer New York: New York, NY, 2013.

(7) Moss, B.; Babacan, O.; Kafizas, A.; Hankin, A. A Review of Inorganic Photoelectrode Developments and Reactor Scale-Up Challenges for Solar Hydrogen Production. *Adv. Energy Mater.* **2021**, *11*, No. 2003286.

(8) Fareza, A. R.; Nugroho, F. A. A.; Abdi, F. F.; Fauzia, V. Nanoscale Metal Oxides−2D Materials Heterostructures for Photoelectrochemical Water Splitting—a Review. *J. Mater. Chem. A* **2022**, *10*, 8656−8686.

(9) Liu, Z.; Cai, Q.; Ma, C.; Zhang, J.; Liu, J. Photoelectrochemical Properties and Growth Mechanism of Varied ZnO Nanostructures. *New J. Chem.* **2017**, *41*, 7947−7952.

(10) Commandeur, D.; Brown, G.; Hills, E.; Spencer, J.; Chen, Q. Defect-Rich ZnO Nanorod Arrays for Efficient Solar Water Splitting. *ACS Appl. Nano Mater.* **2019**, *2*, 1570−1578.

(11) Illy, B. N.; Cruickshank, A. C.; Schumann, S.; Da Campo, R.; Jones, T. S.; Heutz, S.; McLachlan, M. A.; McComb, D. W.; Riley, D. J.; Ryan, M. P. Electrodeposition of ZnO Layers for Photovoltaic Applications: Controlling Film Thickness and Orientation. *J. Mater. Chem.* **2011**, *21*, 12949.

(12) Asadzadeh Patehkhor, H.; Fattahi, M.; Khosravi-Nikou, M. Synthesis and Characterization of Ternary Chitosan−TiO2−ZnO over Graphene for Photocatalytic Degradation of Tetracycline from Pharmaceutical Wastewater. *Sci. Rep.* **2021**, *11*, 24177.

(13) Özgür, Ü.; Alivov, Y. I.; Liu, C.; Teke, A.; Reshchikov, M. A.; Doğan, S.; Avrutin, V.; Cho, S.-J.; Morkoç, H. A Comprehensive Review of ZnO Materials and Devices. *J. Appl. Phys.* **2005**, *98*, No. 041301.

(14) Herron, J. A.; Kim, J.; Upadhye, A. A.; Huber, G. W.; Maravelias, C. T. A General Framework for the Assessment of Solar Fuel Technologies. *Energy Environ. Sci.* **2015**, *8*, 126−157.

(15) Kumar, S.; Kumar, A.; Navakoteswara Rao, V.; Kumar, A.; Shankar, M. V.; Krishnan, V. Defect-Rich MoS_2 Ultrathin Nanosheets-Coated Nitrogen-Doped ZnO Nanorod Heterostructures: An Insight into in-Situ-Generated ZnS for Enhanced Photocatalytic Hydrogen Evolution. *ACS Appl. Energy Mater.* **2019**, *2*, 5622−5634.

(16) Liu, Y.; Weiss, N. O.; Duan, X.; Cheng, H.-C.; Huang, Y.; Duan, X. Van Der Waals Heterostructures and Devices. *Nat. Rev. Mater.* **2016**, *1*, 16042.

(17) Novoselov, K. S.; Mishchenko, A.; Carvalho, A.; Castro Neto, A. H. 2D Materials and van Der Waals Heterostructures. *Science* **2016**, *353*, No. aac9439.

(18) Samadi, M.; Sarikhani, N.; Zirak, M.; Zhang, H.; Zhang, H.-L.; Moshfegh, A. Z. Group 6 Transition Metal Dichalcogenide Nanomaterials: Synthesis, Applications and Future Perspectives. *Nanoscale Horizons* **2018**, *3*, 90−204.
(19) Osterloh, F. E. Inorganic Nanostructures for Photoelectrochemical and Photocatalytic Water Splitting. *Chem. Soc. Rev.* **2013**, *42*, 2294−2320.
(20) Fu, Y.; Wang, Y.; Zhao, H.; Zhang, Z.; An, B.; Bai, C.; Ren, Z.; Wu, J.; Li, Y.; Liu, W.; Li, P.; Ma, J. Synthesis of Ternary ZnO/ZnS/MoS2 Piezoelectric Nanoarrays for Enhanced Photocatalytic Performance by Conversion of Dual Heterojunctions. *Appl. Surf. Sci.* **2021**, *556*, No. 149695.
(21) Su, J.; He, J.; Zhang, J.; Lin, Z.; Chang, J.; Zhang, J.; Hao, Y. Unusual Properties and Potential Applications of Strain BN-MS2 (M = Mo, W) Heterostructures. *Sci. Rep.* **2019**, *9*, 3518.
(22) Ye, J.; Liu, J.; An, Y. Electric Field and Strain Effects on the Electronic and Optical Properties of G-C3N4/WSe2 van Der Waals Heterostructure. *Appl. Surf. Sci.* **2020**, *501*, No. 144262.
(23) Esposito, V.; Castelli, I. E. Metastability at Defective Metal Oxide Interfaces and Nanoconfined Structures. *Adv. Mater. Interfaces* **2020**, *7*, No. 1902090.
(24) Wang, S.; Tian, H.; Ren, C.; Yu, J.; Sun, M. Electronic and Optical Properties of Heterostructures Based on Transition Metal Dichalcogenides and Graphene-like Zinc Oxide. *Sci. Rep.* **2018**, *8*, 12009.
(25) Li, H.; Dong, W.; Zhang, J.; Xi, J.; Du, G.; Ji, Z. MoS_2 Nanosheet/ZnO Nanowire Hybrid Nanostructures for Photoelectrochemical Water Splitting. *J. Am. Ceram. Soc.* **2018**, *101*, 3989−3996.
(26) Jian, W.; Cheng, X.; Huang, Y.; You, Y.; Zhou, R.; Sun, T.; Xu, J. Arrays of ZnO/MoS2 Nanocables and MoS2 Nanotubes with Phase Engineering for Bifunctional Photoelectrochemical and Electrochemical Water Splitting. *Chem. Eng. J.* **2017**, *328*, 474−483.
(27) Nguyen, T. D.; Man, M. T.; Nguyen, M. H.; Seo, D.; Kim, E. Effect of Few-Layer MoS2 Flakes Deposited ZnO/FTO Nanorods on Photoelectrochemical Characteristic. *Mater. Res. Express* **2019**, *6*, No. 085070.
(28) Trung, T. N.; Seo, D.-B.; Quang, N. D.; Kim, D.; Kim, E.-T. Enhanced Photoelectrochemical Activity in the Heterostructure of Vertically Aligned Few-Layer MoS2 Flakes on ZnO. *Electrochim. Acta* **2018**, *260*, 150−156.
(29) Shi, J.-W.; Ma, D.; Zou, Y.; Fan, Z.; Shi, J.; Cheng, L.; Ji, X.; Niu, C. Rational Construction of Multiple Interfaces in Ternary Heterostructure for Efficient Spatial Separation and Transfer of Photogenerated Carriers in the Application of Photocatalytic Hydrogen Evolution. *J. Power Sources* **2018**, *379*, 249−260.
(30) Ma, D.; Shi, J.-W.; Zou, Y.; Fan, Z.; Shi, J.; Cheng, L.; Sun, D.; Wang, Z.; Niu, C. Multiple Carrier-Transfer Pathways in a Flower-like In 2 S 3/CdIn 2 S 4/In 2 O 3 Ternary Heterostructure for Enhanced Photocatalytic Hydrogen Production. *Nanoscale* **2018**, *10*, 7860−7870.
(31) Li, F.; Zhang, D.; Xu, R.-C.; Fu, W.-F.; Lv, X.-J. Superhydrophilic Heteroporous MoS_2/Ni_3S_2 for Highly Efficient Electrocatalytic Overall Water Splitting. *ACS Appl. Energy Mater.* **2018**, *1*, 3929−3936.
(32) Liu, Y.; Sun, J.; Lin, S.; Xu, Z.; Li, L. In-Situ Growth of Interconnected NiS2/MoS2 Nanowires Supported on Ni Foam as Binder-Free Electrode for Hybrid Supercapacitor. *J. Alloys Compd.* **2020**, *820*, No. 153113.
(33) Pan, L.; Jiao, C.; Liang, Y.; Xiong, J.; Wang, S.; Zhu, H.; Chen, G.; Song, H. In Situ Construction of MoS2@CoS2 Spherical Hydrangea-Shaped Clusters for Enhanced Visible-Light Photocatalytic Degradation of Sulfamethoxazole. *New J. Chem.* **2021**, *45*, 5645−5653.
(34) Zhou, W.; Yin, Z.; Du, Y.; Huang, X.; Zeng, Z.; Fan, Z.; Liu, H.; Wang, J.; Zhang, H. Synthesis of Few-Layer MoS_2 Nanosheet-Coated TiO_2 Nanobelt Heterostructures for Enhanced Photocatalytic Activities. *Small* **2013**, *9*, 140−147.
(35) Li, L.; King, D. L. H2S Removal with ZnO during Fuel Processing for PEM Fuel Cell Applications. *Catal. Today* **2006**, *116*, 537−541.
(36) Senthil Kumar, S. M.; Selvakumar, K.; Thangamuthu, R.; Karthigai Selvi, A.; Ravichandran, S.; Sozhan, G.; Rajasekar, K.; Navascues, N.; Irusta, S. Hydrothermal Assisted Morphology Designed MoS 2 Material as Alternative Cathode Catalyst for PEM Electrolyser Application. *Int. J. Hydrogen Energy* **2016**, *41*, 13331−13340.
(37) Chubarov, M.; Choudhury, T. H.; Zhang, X.; Redwing, J. M. In-Plane x-Ray Diffraction for Characterization of Monolayer and Few-Layer Transition Metal Dichalcogenide Films. *Nanotechnology* **2018**, *29*, No. 055706.
(38) Consonni, V.; Lord, A. M. Polarity in ZnO Nanowires: A Critical Issue for Piezotronic and Piezoelectric Devices. *Nano Energy* **2021**, *83*, No. 105789.
(39) Pawar, A. U.; Kim, C. W.; Kang, M. J.; Kang, Y. S. Crystal Facet Engineering of ZnO Photoanode for the Higher Water Splitting Efficiency with Proton Transferable Nafion Film. *Nano Energy* **2016**, *20*, 156−167.
(40) Meng, X.; Xiao, H.; Wen, X.; Goddard, W. A., III; Li, S.; Qin, G. Dependence on the Structure and Surface Polarity of ZnS Photocatalytic Activities of Water Splitting: First-Principles Calculations. *Phys. Chem. Chem. Phys.* **2013**, *15*, 9531.
(41) Banerjee, P.; Jain, P. K. Mechanism of Sulfidation of Small Zinc Oxide Nanoparticles. *RSC Adv.* **2018**, *8*, 34476−34482.
(42) Ma, D.; Shi, J.-W.; Sun, D.; Zou, Y.; Cheng, L.; He, C.; Wang, H.; Niu, C.; Wang, L. Au Decorated Hollow ZnO@ZnS Heterostructure for Enhanced Photocatalytic Hydrogen Evolution: The Insight into the Roles of Hollow Channel and Au Nanoparticles. *Appl. Catal., B* **2019**, *244*, 748−757.
(43) Tang, C.; Chen, C.; Zhang, H.; Zhang, J.; Li, Z. Enhancement of Degradation for Nitrogen Doped Zinc Oxide to Degrade Methylene Blue. *Phys. B* **2020**, *583*, No. 412029.
(44) Majumder, T.; Dhar, S.; Chakraborty, P.; Debnath, K.; Mondal, S. P. Advantages of ZnO Nanotaper Photoanodes in Photoelectrochemical Cells and Graphene Quantum Dot Sensitized Solar Cell Applications. *J. Electroanal. Chem.* **2018**, *813*, 92−101.
(45) Yin, D.; Wang, M.-L.; Wang, Y.-Z.; Hu, X.; Liu, B.; Liu, H.; Ma, L.; Gao, G.-G. A Ternary ZnO/ZnS/MoS_2 Composite as a Reusable SERS Substrate Derived from the Polyoxomolybdate/ZIF-8 Host−Guest Framework. *J. Mater. Chem. C* **2019**, *7*, 9856−9864.
(46) Chen, Q.; Wang, H.; Luan, Q.; Duan, R.; Cao, X.; Fang, Y.; Ma, D.; Guan, R.; Hu, X. Synergetic Effects of Defects and Acid Sites of 2D-ZnO Photocatalysts on the Photocatalytic Performance. *J. Hazard. Mater.* **2020**, *385*, No. 121527.
(47) Ali, A.; Rahman, G.; Ali, T.; Nadeem, M.; Hasanain, S. K.; Sultan, M. Enhanced Band Edge Luminescence of ZnO Nanorods after Surface Passivation with ZnS. *Phys. E* **2018**, *103*, 329−337.
(48) Chang, C.-J.; Chen, J.-K.; Lin, K.-S.; Huang, C.-Y.; Huang, C.-L. Improved H2 Production of ZnO@ZnS Nanorod-Decorated Ni Foam Immobilized Photocatalysts. *Int. J. Hydrogen Energy* **2021**, *46*, 11357−11368.
(49) Fan, X.; Xu, P.; Zhou, D.; Sun, Y.; Li, Y. C.; Nguyen, M. A. T.; Terrones, M.; Mallouk, T. E. Fast and Efficient Preparation of Exfoliated 2H MoS_2 Nanosheets by Sonication-Assisted Lithium Intercalation and Infrared Laser-Induced 1T to 2H Phase Reversion. *Nano Lett.* **2015**, *15*, 5956−5960.
(50) Zheng, J.; Zhang, H.; Dong, S.; Liu, Y.; Tai Nai, C.; Suk Shin, H.; Young Jeong, H.; Liu, B.; Ping Loh, K. High Yield Exfoliation of Two-Dimensional Chalcogenides Using Sodium Naphthalenide. *Nat. Commun.* **2014**, *5*, 2995.
(51) Chen, S.; Huang, D.; Xu, P.; Xue, W.; Lei, L.; Cheng, M.; Wang, R.; Liu, X.; Deng, R. Semiconductor-Based Photocatalysts for Photocatalytic and Photoelectrochemical Water Splitting: Will We Stop with Photocorrosion? *J. Mater. Chem. A* **2020**, *8*, 2286−2322.
(52) Laszczyńska, A.; Szczygieł, I. Electrocatalytic Activity for the Hydrogen Evolution of the Electrodeposited Co−Ni−Mo, Co−Ni

https://doi.org/10.1021/acsanm.2c01434
ACS Appl. Nano Mater. 2022, 5, 16051−16060

and Co−Mo Alloy Coatings. *Int. J. Hydrogen Energy* **2020**, *45*, 508−520.
(53) Molero-Sánchez, B.; Prado-Gonjal, J.; Ávila-Brande, D.; Chen, M.; Morán, E.; Birss, V. High Performance La 0.3 Ca 0.7 Cr 0.3 Fe 0.7 O 3−δ Air Electrode for Reversible Solid Oxide Fuel Cell Applications. *Int. J. Hydrogen Energy* **2015**, *40*, 1902−1910.
(54) Wang, G.; Ling, Y.; Wang, H.; Xihong, L.; Li, Y. Chemically Modified Nanostructures for Photoelectrochemical Water Splitting. *J. Photochem. Photobiol., C* **2014**, *19*, 35−51.
(55) Wheeler, D. A.; Wang, G.; Ling, Y.; Li, Y.; Zhang, J. Z. Nanostructured Hematite: Synthesis, Characterization, Charge Carrier Dynamics, and Photoelectrochemical Properties. *Energy Environ. Sci.* **2012**, *5*, 6682.
(56) Kumar, S.; Ahirwar, S.; Satpati, A. K. Insight into the PEC and Interfacial Charge Transfer Kinetics at the Mo Doped $BiVO_4$ Photoanodes. *RSC Adv.* **2019**, *9*, 41368−41382.
(57) Zhang, K.; Dong, T.; Xie, G.; Guan, L.; Guo, B.; Xiang, Q.; Dai, Y.; Tian, L.; Batool, A.; Jan, S. U.; Boddula, R.; Thebo, A. A.; Gong, J. R. Sacrificial Interlayer for Promoting Charge Transport in Hematite Photoanode. *ACS Appl. Mater. Interfaces* **2017**, *9*, 42723−42733.
(58) Brayek, A.; Chaguetmi, S.; Ghoul, M.; Ben Assaker, I.; Souissi, A.; Mouton, L.; Beaunier, P.; Nowak, S.; Mammeri, F.; Chtourou, R.; Ammar, S. Photoelectrochemical Properties of Nanocrystalline ZnS Discrete versus Continuous Coating of ZnO Nanorods Prepared by Electrodeposition. *RSC Adv.* **2016**, *6*, 30919−30927.
(59) Hassan, M. A.; Waseem, A.; Johar, M. A.; Bagal, I. V.; Ha, J.-S.; Ryu, S.-W. Single-Step Fabrication of 3D Hierarchical ZnO/ZnS Heterojunction Branched Nanowires by MOCVD for Enhanced Photoelectrochemical Water Splitting. *J. Mater. Chem. A* **2020**, *8*, 8300−8312.
(60) Madkour, M.; Al Sagheer, F. Au/ZnS and Ag/ZnS Nano-heterostructures as Regenerated Nanophotocatalysts for Photo-catalytic Degradation of Organic Dyes. *Opt. Mater. Express* **2017**, *7*, 158.
(61) Tian, Q.; Wu, W.; Yang, S.; Liu, J.; Yao, W.; Ren, F.; Jiang, C. Zinc Oxide Coating Effect for the Dye Removal and Photocatalytic Mechanisms of Flower-Like MoS2 Nanoparticles. *Nanoscale Res. Lett.* **2017**, *12*, 221.
(62) Bengas, R.; Lahmar, H.; Redha, K. M.; Mentar, L.; Azizi, A.; Schmerber, G.; Dinia, A. Electrochemical Synthesis of N-Type ZnS Layers on p-Cu 2 O/n-ZnO Heterojunctions with Different Deposition Temperatures. *RSC Adv.* **2019**, *9*, 29056−29069.
(63) Lee, G.-C.; Lyu, L.-M.; Hsiao, K.-Y.; Huang, Y.-S.; Perng, T.-P.; Lu, M.-Y.; Chen, L.-J. Induction of a Piezo-Potential Improves Photocatalytic Hydrogen Production over ZnO/ZnS/MoS2 Hetero-structures. *Nano Energy* **2022**, *93*, No. 106867.
(64) Liu, Y.; Xie, S.; Li, H.; Wang, X. A Highly Efficient Sunlight Driven ZnO Nanosheet Photocatalyst: Synergetic Effect of P-Doping and MoS_2 Atomic Layer Loading. *ChemCatChem* **2014**, *6*, 2522−2526.
(65) Xue, F.; Chen, L.; Chen, J.; Liu, J.; Wang, L.; Chen, M.; Pang, Y.; Yang, X.; Gao, G.; Zhai, J.; Wang, Z. L. P-Type MoS_2 and n-Type ZnO Diode and Its Performance Enhancement by the Piezophototronic Effect. *Adv. Mater.* **2016**, *28*, 3391−3398.

https://doi.org/10.1021/acsanm.2c01434
ACS Appl. Nano Mater. 2022, 5, 16051−16060